Lawrence Berkeley National Laboratory
Recent Work

Title
Observationally derived rise in methane surface forcing mediated by water vapour trends

Permalink
https://escholarship.org/uc/item/5gc4b6cg

Journal
Nature Geoscience, 11(4)

ISSN
1752-0894

Authors
Feldman, DR
Collins, WD
Biraud, SC
et al.

Publication Date
2018-04-01

DOI
10.1038/s41561-018-0085-9

Peer reviewed

1 **Title:**

2 Observationally-derived rise in methane surface forcing mediated by water vapour trends

3

4 **Author Information:**

5 D.R. Feldman[1]*, W.D. Collins[1,2] ‡, S.C. Biraud[1], M.D. Risser[1], D.D. Turner[3], P.J. Gero[4], J.

6 Tadić[1], D. Helmig[5], S. Xie[6], E.J. Mlawer[7], T.R Shippert[8] and M.S. Torn[1,2]

7 **Affiliations:**

8 [1] Lawrence Berkeley National Laboratory, Berkeley, CA, USA.

9 [2] University of California-Berkeley, Berkeley, CA, USA.

10 [3] National Oceanic and Atmospheric Administration Earth Systems Research Laboratory,

11 Boulder, CO, USA.

12 [4] University of Wisconsin-Madison, Madison, WI, USA.

13 [5] Institute of Arctic and Alpine Research, University of Colorado-Boulder, Boulder, CO, USA.

14 [6] Lawrence Livermore National Laboratory, Livermore, CA, USA.

15 [7] Atmospheric and Environmental Research, Lexington, MA, USA.

16 [8] Pacific Northwest National Laboratory, Richland, WA, USA.

17

18 *Corresponding Author:1 Cyclotron Road, MS 74R-316C, Berkeley, CA 94720, USA.

19 drfeldman@lbl.gov

20 ‡ Denotes co-lead author.

Main Text:

Atmospheric methane (CH_4) mixing ratios exhibited a plateau between 1995 and 2006 and have been subsequently increasing. While there are a number of competing explanations for the temporal evolution of this greenhouse gas, these prominent features in the temporal trajectory of atmospheric CH_4 are expected to perturb the surface energy balance through radiative forcing, largely due to CH_4's infrared radiative absorption features. However, to date this has been determined strictly through radiative transfer calculations. Here, we present a quantified observation of the time-series of clear-sky radiative forcing by CH_4 at the surface from 2002-2012 at a single site derived from spectroscopic measurements along with line-by-line calculations using ancillary data. There was no significant trend in CH_4 forcing between 2002 and 2006, but since then, the trend in forcing was 0.026±0.09 (99.7% CI) W/m^2/yr. The seasonal-cycle amplitude and secular trends in observed forcing are influenced by a corresponding seasonal cycle and trend in atmospheric CH_4. However, we find that we must account for the overlapping absorption effects of atmospheric water vapour (H_2O) and CH_4 to explain the observations fully. Thus, the determination of CH_4 radiative forcing requires accurate observations of both the spatiotemporal distribution of CH_4 and the vertically resolved trends in H_2O.

Atmospheric CH_4 and Its Radiative Forcing

The globally-averaged atmospheric mixing ratio of CH_4 has risen since the pre-industrial epoch from 722±25 ppbv in 1750 to 1803±2 ppbv in 2011[1]. However, there is an unresolved debate regarding the causes of the temporal trajectory of CH_4, and thus its sources and sinks, over the last 30 years. The observed plateau in the CH_4 mixing ratio[2] and its end[3] have been attributed to

44   some combination of changes in (1) hydroxyl (OH) radical destruction, (2) tropical wetland

45   emissions, (3) thawing permafrost and CH_4 hydrates, (4) agriculture, and (5) fossil-fuel

46   extraction and use, though their relative contributions are ambiguous given existing

47   observations[4-10].

48

49   Rising atmospheric CH_4 mixing ratios are expected to change the distribution of atmospheric

50   radiative energy, and this is the essential justification for coordinated and prioritized scientific

51   inquiry regarding atmospheric CH_4. While substantial resources have been devoted to measuring

52   increasing atmospheric CH_4[2,11] and understanding its anthropogenic contributions[12-14], the

53   observational determination of its radiative forcing has, to date, been limited. Satellite

54   observations have inferred, but not quantified, the radiative forcing associated with rising mixing

55   ratios of this gas[15,16]. Apart from those efforts, radiative forcing values have been strictly

56   calculated by radiative transfer models based on information gathered from laboratory

57   observations. The calculations performed for the IPCC Fifth Assessment report found that CH_4

58   has contributed to a stratospherically-adjusted longwave (5-20 μm) radiative forcing at the

59   tropopause of 0.48 ± 0.05 W/m^2 from the pre-industrial epoch[1]. However, the methods used by

60   that report were last revised in 1998[17], and recent work has indicated that an upward revision to

61   the methane radiative forcing formulae and the determination of its global warming potential for

62   future Assessment Reports is necessary[18], mostly due to the need to include shortwave effects.

63

64   The spectroscopy of CH_4, which is the foundation underlying the radiative forcing calculations,

65   is an active area of research[19]. This is because CH_4 exhibits a line structure of exceptional

66   complexity compared to other atmospheric greenhouse gases[20], and line-by-line calculations and

67   climate model radiation codes must capture this complexity to determine CH_4 radiative forcing.

68   They do so by using line parameters in spectroscopic databases such as High Resolution

69   Transmission (HITRAN)[21] and parameterizations of other absorption effects. These databases

70   are frequently updated, and while the updates have produced only modest changes in CH_4

71   infrared forcing[22,23], the scientific understanding of other potentially significant absorption

72   effects such as broadening dependencies[24] and H_2O continuum absorption[18,25] is still advancing.

73   Alternatively, we can use field observations to establish the sufficiency of the approach by which

74   CH_4 radiative forcing is solely determined from radiative transfer calculations.

75

76   The specialized, long-duration suite of observations collected at the U.S. Department of Energy

77   Atmospheric Radiation Measurement (ARM) Program[26] at the Southern Great Plains (SGP) site

78   (36° 36′ 18″ N, 97° 29′ 6″ W) provide a unique opportunity to observe greenhouse gases and

79   their forcing, as indicated by the first observation of the increase in the greenhouse effect from

80   rising atmospheric concentrations of CO_2[(27)].

81

82   The time-series of weekly CH_4 surface flask measurements from SGP shows a high variability in

83   CH_4 at SGP, with boundary layer excursions sometimes exceeding 2300 ppbv (Figure 1). As

84   with other locations of high-precision atmospheric CH_4 measurements, the time-series of CH_4

85   mixing ratios shows fine-scale temporal variability. At SGP, some of the excursions may be due

86   to local hydrocarbon recovery, based on the correlation between CH_4 and ethane mixing

87   ratios[28,29] (see Methods). Meanwhile, an analysis of these instantaneous CH_4 observations (see

88   Methods) shows (1) no significant trend in atmospheric CH_4 before 2007, (2) a break-point in

89   2007, and (3) that CH_4 mixing ratios have been rising at a rate of 7.5±4.4 (95% CI) ppbv/yr since

90   then.

91

92   While other studies have observed trends in the surface energy balance with broadband

93   radiometry[30,31], broadband observations are inadequate for attributing changes in that balance to

94   changes in atmospheric composition of specific gas species. Therefore, we use a long time-series

95   of clear-sky downwelling spectral infrared radiance observations to determine if changes in

96   atmospheric CH_4 mixing ratios have a discernible effect on the surface energy balance. We focus

97   here on longwave clear-sky flux changes since they are predicted to be the most sensitive

98   longwave radiative flux signal associated with rising greenhouse gases[32] and since detailed all-

99   sky forcing calculations of the study site indicate that most of the forcing arises under clear-sky

100   conditions (see Methods).

101

102   **CH_4 Radiative Forcing Dependencies**

103   Figure 2(a) shows, through radiative transfer calculations, that the infrared emission by CH_4 that

104   contributes to its longwave surface radiative forcing occurs predominantly between 1200 and

105   1350 cm^{-1}. However, as the radiative transfer calculations in Figure 2(b) show, the determination

106   of CH_4 forcing is complicated by a significant H_2O and N_2O dependence of the downwelling

107   flux in the CH_4 absorption band, arising from the overlap of spectral absorption features of H_2O

108   and N_2O with those of CH_4. The downwelling flux is also highly temperature-dependent both

109   due to Planck function and absorption line temperature dependence. Fortunately, the surface

110   mixing ratios for N_2O are highly correlated with its mixing ratios throughout the column (Figure

111   2(c)), so the radiative effects of N_2O can be estimated using a near-surface measurement of its

112   mixing ratio. Radiosonde data at the ARM SGP site were used to control for variability in the

113   atmospheric thermodynamic state[33]. Airborne measurements indicate that boundary-layer and

114   free tropospheric fluctuations in CH_4 mixing ratios are not highly correlated at subseasonal time-

115   scales. Therefore, surface observations of CH_4 mixing ratio alone are insufficient for calculating

116   CH_4 forcing at the time-scales of our analysis.

117

118   CH_4 surface radiative forcing was derived from 11 years' of infrared spectroscopic observations

119   made by the Atmospheric Emitted Radiance Interferometer (AERI)[34]. The forcing was

120   determined by differencing AERI measurements with counterfactual line-by-line calculations[27]

121   where the thermodynamic state is prescribed by concurrent radiosonde observations[33], but the

122   calculation used a pre-industrial CH_4 mixing ratio (see Methods). Detailed data quality control

123   and averaging methods were used to account for the effects of uncertainties in temperature, H_2O,

124   and N_2O, and the effect of instrumental noise, respectively (see Methods). The minimum

125   temporal resolution of the observations used here was 6 hours (see Methods). From this process

126   chain, we observe the direct, unadjusted, instantaneous radiative forcing at the surface, which,

127   while not biased by the effects of thermodynamics (see Methods), is still affected by them.

128   Ideally, measurements would be made under prescribed thermodynamic conditions, but we have

129   no means of controlling for these conditions in the field.

130

131   The mean spectral residuals were prominent only in the spectral region of CH_4 absorption (see

132   Methods) and therefore exclude the possibility that uncertainties in the atmospheric state and

133   instrument calibration were substantially affecting the results. Top-down validation of our

134   forcing estimates, based on *in situ* observations by simultaneous aircraft overflights[35], indicates

135   that we can observe instantaneous CH_4 forcing to within 0.14 W/m^2 (see Methods). Sensitivity

136   tests (see Methods) reveal that the transient plumes of boundary layer methane would lead to an

137   instantaneous surface radiative forcing signal of 0.05 W/m^2, so our analysis is unable to discern

138   the transient contribution of anthropogenic activity to observed forcing. However, supraseasonal

139   time-series features of atmospheric CH_4 mixing ratios, which do contain contributions from

140   human activity[4-10], are readily discernible in the observed radiative forcing.

141

142   **Observationally-Derived Forcing Time-Series and Influence of Thermodynamics**

143   Irrespective of the source of the atmospheric CH_4, we derive a time-series of CH_4 surface

144   longwave radiative forcing from observations that exhibits several prominent features (Figure 3).

145   During the multi-year atmospheric CH_4 plateau, the trend in this forcing did not differ

146   significantly from zero (p>0.1). The time-series exhibited a significant change around 2007 at

147   the end of the plateau (p<0.0001). From then onwards, the trend differed from zero at

148   0.026±0.006 W/m^2/yr (99.7% CI). During the 11-year record, there was a large seasonal cycle,

149   with an amplitude of at least 0.2 W/m^2.

150

151   During the time period of the atmospheric CH_4 plateau, it is expected that there would not be

152   significant trends in surface radiative forcing from CH_4, and this was confirmed by observations.

153   However, the amplitude of the seasonal cycle in surface forcing throughout the time-series and

154   the forcing trend since 2006 cannot be fully explained by the atmospheric CH_4 mixing ratio at

155   SGP. The amplitude of the seasonal cycle in CH_4 dry atmospheric mixing ratio is 51.2±10.1

156   (99.7% CI) ppbv, and, based on the mean water vapor profile during the observational period at

157   the SGP, the seasonal cycle amplitude would be 0.012±0.002 (99.7% CI) W/m^2, significantly

158   smaller than the observed amplitude of 0.25±0.01 (99.7% CI) W/m^2. The observed trend in CH_4

159   since 2007 is 7.5±6.6 (99.7% CI) ppbv/yr which, again based on the mean water vapor profile

160   during the observational period at the SGP, would yield a trend of 0.002±0.0009 (99.7% CI)

161   W/m^2/yr, significantly smaller than the observed trend of 0.026±0.006 (99.7% CI) W/m^2/yr.

162   However, analyzing the time-series in isolation from thermodynamics is highly idealized, can

163   yield varying results depending on the choice of thermodynamic conditions, and is inconsistent

164   with actual conditions in the field. Nevertheless, this discrepancy must be resolved.

165

166   We can exclude several potential explanations for these findings; for example, the contributions

167   of observational error and analysis error would produce spectral residuals outside of the CH_4

168   absorption band and time-series statistics that are inconsistent with our findings. Possible

169   contributions from other radiatively-active trace gases in the CH_4 absorption band between 1200

170   and 1350 cm^{-1} can also be excluded (see Methods).

171

172   Rather, we find that when we perform a multivariate signal decomposition analysis of the

173   deseasonalized time-series of CH_4 forcing constructed over the entire time-series using a

174   nonlinear predictor based solely on CH_4 concentrations, we can explain roughly 80% of the

175   variation in observed forcing (R^2=0.793), implying that at least 20.7% of the variance is related

176   to other factors (see Methods).

177

178   Rather, we find that the contribution of trends and variability in water vapour to those in CH_4

179   surface forcing are significant. Even though the residual spectra indicate that we are not

180   imprecisely specifying atmospheric temperature and moisture, CH_4 forcing is nonetheless

181   dependent on atmospheric state. The primary reason for this water vapour dependence is that

182   mid-IR CH_4 absorption occurs at the edge of a strong v_2 H_2O absorption band. Therefore,

183   elevated H_2O mixing ratios saturate the CH_4 band[36] and reduce the latter molecule's radiative

184   forcing, as shown in Figures 4(d). Indeed, we performed a model-only computation based on

185   observed thermodynamics and CH_4 mixing ratios and obtain a trend of 0.020±0.009 (99.7% CI)

186    $W/m^2/yr$, which is not distinguishable ($p > 0.05$) from the observationally-derived trend.

187   Additionally, this effect is largely insensitive to the observed mid-tropospheric temperature

188   changes, as shown in Figure 4(c).

189

190   For the seasonal cycle, we find that the water vapour seasonal cycle of 7.7±0.03 g/kg helps

191   explain the seasonal cycle in observed CH_4 surface forcing. For trends, we note that a long-term

192   decreasing trend in moisture availability in the central US has been observed[37]. This was also

193   observed in a 14-year analysis of AERI clear-sky radiances[38]. At SGP, an analysis of radiosondes

194   coincidental to the CH_4 forcing observations is consistent with that finding and yields negative

195   trends in atmospheric moisture in the lowest 1 km, as shown in Figure 4(b). While no significant

196   change point in the vertically-resolved time-series is observed, column water decreased by 30%

197   since the end of the CH_4 plateau. This negative trend over the entire time-series and especially

198   since the end of the CH_4 plateau will tend to enhance CH_4 forcing, and provides the opportunity

199   to analyze the alternating effects of CH_4 and H_2O on the observed forcing. Figure 5 shows that

200   the observed forcing trends in CH_4 forcing could be reproduced only when we include nonlinear

201   predictors that include both CH_4 concentration and observed thermodynamic trends ($R^2 = 0.997$,

202   see Methods). Specifically, trends in CH_4 surface flask measurements and trends in height-

203   resolved temporal profiles of temperature and humidity can be used to predict both plateau and

204 post-plateau surface radiative forcing trends after all variables are decomposed into frequency

205 noise (5a), a seasonal component (5b), and deseasonalized trends (5c), yielding a normally-

206 distributed residual signal (5d). The result is that the first temperature and moisture principal

207 components, covering the lower 5 km of the atmosphere, explain nearly all of the signal's

208 variance (5e and 5f).

209

210 **Broader Implications**

211 This study presents the first observational derivation and quantification of the effect of time-

212 varying CH_4 on the clear-sky surface energy balance, with a large seasonal cycle amplitude of

213 0.25 W/m^2 and a significant difference in forcing trends at SGP during and after the CH_4 plateau.

214 The decadally-averaged trend in surface forcing was larger for CO_2 than CH_4 at this site, but the

215 perturbation of the surface energy balance from rising CH_4 mixing ratios since the end of the

216 plateau was similar to the effect from rising CO_2 (0.02±0.007 W/m^2/yr) at the site. Though this

217 difference was not statistically significant (p>0.3), it suggests that, since the end of the plateau,

218 the role of rising CH_4 in perturbing the surface energy balance can be highly dependent on local

219 water vapour trends[39-42]. At SGP, CH_4 surface forcing trends are not necessarily inferior to that

220 of CO_2, even though forcing at tropopause by CO_2 is much more than CH_4[(1)].

221

222 These observations show a long-term trend in CH_4 surface radiative forcing, with variance from

223 a function of rising CH_4 mixing ratios and the non-negligible contribution that depends on the

224 vertical distribution of water vapour. This finding is related to tropopausal radiative forcing,

225 which figures prominently in the scientific discussion of how rising CH_4 impacts average

226 tropospheric temperatures[1], but spatial patterns in upper tropospheric moisture[43] mediate forcing

227   at the tropopause, while surface humidity more strongly affects surface forcing. For this

228   investigation, we find that trends in surface forcing from greenhouse gases are convolved with

229   the details of how the thermodynamic state of the atmosphere is evolving, and the local

230   thermodynamic conditions must be taken into account. Since local temperature and humidity

231   trends that are distinct from those at SGP exist at other sites, the relative contributions of

232   thermodynamics and mixing ratio changes to the forcing may also differ. Observed trends in

233   surface humidity have not been spatially or temporally uniform, nor have they been monotonic.

234   The magnitude of the globally-averaged land-surface humidity trend varies on decadal time-

235   scales while also exhibiting trends that are spatially variable over land and that show strong land-

236   ocean contrast[39-42]. Therefore, the direct impact of greenhouse gases on the surface energy

237   balance cannot be predicted in isolation from thermodynamics. Nevertheless, as we have shown,

238   CH_4 surface radiative forcing trends can be derived from measurements and quantified

239   spectroscopically.

240 **References:**

241 1. Myhre, G., *et al*. *Climate Change 2013: The Physical Science Basis. Contribution of*

242 *Working Group I to the Fifth Assessment Report of the Intergovernmental Panel on*

243 *Climate Change Ch. 8* (Cambridge University Press, Cambridge, United Kingdom and

244 New York, NY, USA, 2013).

245 2. Dlugokencky, E.J., Nisbet, E.G., Fisher, R. & Lowry, D. Global atmospheric methane:

246 budget, changes and dangers. *Philos. Trans. R. Soc. London Ser. A.* **369,** 2058-2072

247 (2011).

248 3. Nisbet, E.G., Dlugokencky, E.J. & Bousquet, P. Methane on the rise—again. *Science*

249 **343,** 493-495 (2014).

250 4. Kirschke, S., *et al*. Three decades of global methane sources and sinks. *Nat. Geosci.* **6,**

251 813-823 (2013).

252 5. Aydin, M., *et al*. Recent decreases in fossil-fuel emissions of ethane and methane derived

253 from firn air. *Nature* **476,** 198-201 (2011).

254 6. Kai, F.M., Tyler, S.C., Randerson, J.T. & Blake, D.R. Reduced methane growth rate

255 explained by decreased Northern Hemisphere microbial sources. *Nature* **476,** 194-197

256 (2011).

257 7. Schaefer, H., *et al*. A 21st century shift from fossil-fuel to biogenic methane emissions

258 indicated by $^{13}CH_4$. *Science* **352,** 80-84 (2016).

259 8. Prather, M.J. & Holmes, C.D. Overexplaining or underexplaining methane's role in

260 climate change. *Proc. Natl. Acad. Sci. USA*. **114,** 5324-5326 (2017).

261 9. Rigby M, *et al*. Role of atmospheric oxidation in recent methane growth. *Proc Natl.*

262 *Acad. Sci. USA*. **114,** 5373–5377 (2017).

263   10. Turner, A.J., Frankenberg, C., Wennberg, P.O. & Jacob, D.J. Ambiguity in the causes for

264   decadal trends in atmospheric methane and hydroxyl. *Proc Natl. Acad. Sci. USA*. **114,**

265   5367–5372 (2017).

266   11. Bergamaschi, P., *et al*. Atmospheric CH_4 in the first decade of the 21st century: Inverse

267   modeling analysis using SCIAMACHY satellite retrievals and NOAA surface

268   measurements. *J. Geophys. Res.* **118,** 7350–7369 (2013).

269   12. Turner, A.J., *et al.* A large increase in U.S. methane emissions over the past decade

270   inferred from satellite data and surface observations. *Geophys. Res. Lett.* **43,** 2218-2224

271   (2016).

272   13. Miller, S.M., *et al*. Anthropogenic emissions of methane in the United States. *Proc. Natl.*

273   *Acad. Sci. USA*. **110,** 20018-20022 (2013).

274   14. Brandt, A.R., *et al.* Methane leaks from North American natural gas systems. *Science*.

275   **343,** 733-735 (2014).

276   15. Harries, J.E., Brindley, H.E., Sagoo, P.J. & Bantges. R.J. Increases in greenhouse gas

277   forcing inferred from outgoing longwave spectra of the Earth in 1970 and 1997. *Nature*

278   **410**, 355-357 (2001).

279   16. Griggs, J.A. & Harries, J.E. Comparison of spectrally resolved outgoing longwave

280   radiation over the tropical Pacific between 1970 and 2003 using IRIS, IMG, and AIRS. *J.*

281   *Climate* **20,** 3982-4001 (2007).

282   17. Myhre, G., Highwood, E.J., Shine, K.P. & Stordal, F. New estimates of radiative forcing

283   due to well mixed greenhouse gases. *Geophys. Res. Lett.* **25,** 2715-2718 (1998).

284   18. Etminan, M., Myhre, G., Highwood, E.J. & Shine, K.P. Radiative forcing of carbon

285   dioxide, methane, and nitrous oxide: A significant revision of the methane radiative

286   forcing. *Geophys. Res. Lett.* **43,** 12614-12623 (2016).

287   19. Brown, L.R., *et al*. Methane line parameters in the HITRAN2012 database. *J. Quant.*

288   *Spectrosc. Rad. Trans.* **130,** 201-219 (2013).

289   20. Goody, R.M. & Yung, Y.L. *Atmospheric Radiation: Theoretical Basis Ch. 3* (Oxford

290   Univ. Press, New York, 1989).

291   21. Rothman, L.S., *et al*. The HITRAN2012 molecular spectroscopic database. *J. Quant.*

292   *Spectrosc. Rad. Trans.* **130,** 4-50 (2013).

293   22. Kratz, D.P. The sensitivity of radiative transfer calculations to the changes in the

294   HITRAN database from 1982 to 2004. *J. Quant. Spectrosc. Rad. Trans.* **109,** 1060-1080,

295   (2008).

296   23. Lu, P., Zhang, H. & Jing, X. The effects of different HITRAN versions on calculated

297   long-wave radiation and uncertainty evaluation. *Acta Meteor. Sin.* **26,** 389-398 (2012).

298   24. Delahaye, T, *et al*. Measurements of H_2O broadening coefficients of infrared methane

299   lines. *J. Quant. Spectrosc. Rad. Trans.* **173,** 40–48 (2016).

300   25. Mlawer, E. J., *et al.* Development and recent evaluation of the MT_CKD model of

301   continuum absorption. *Phil. Trans. Roy. Soc. A*. **370,** 1-37 (2012).

302   26. Turner, D.D. & Ellingson, R.G. *The Atmospheric Radiation Measurement Program: The*

303   *First 20 Years*, (Amer. Meteor. Soc., Boston, 2016).

304   27. Feldman, D.R., *et al*. Observational determination of surface radiative forcing by CO_2

305   from 2000 to 2010. *Nature* **519,** 339-343 (2015).

306   28. Helmig, D., *et al*. Reversal of global atmospheric ethane and propane trends largely due

307   to US oil and natural gas production. *Nature Geo.* **9,** 490-495 (2016).

308   29. Hausmann, P., Sussmann, R., & Smale, D. Contribution of oil and natural gas production

309   to renewed increase in atmospheric methane (2007-2014): top-down estimate from ethane

310   and methane column observations. *Atmos. Chem. Phys.* **16,** 3227-3244 (2016).

311   30. Wild, M., et al. The global energy balance from a surface perspective. *Clim. Dynam.* **40,**

312   3107-3134 (2013).

313   31. Wang, K. & Liang, S. Global atmospheric downward longwave radiation over land

314   surface under all-sky conditions from 1973 to 2008. *J. Geophys. Res.* **114,** D19101,

315   (2009).

316   32. Stephens, G.L., *et al*. An update on Earth's energy balance in light of the latest global

317   observations. *Nature Geosci.* **5,** 691–696 (2012).

318   33. Xie, S., *et al*. Clouds and more: ARM Climate Modeling Best Estimate Data. *Bull. Amer.*

319   *Meteor. Soc.* **91,** 31-20 (2010).

320   34. Knuteson, R.O., *et al*. Atmospheric Emitted Radiance Interferometer. Part I: Instrument

321   design. *J. Atmos. Ocean. Technol.* **21,** 1763–1776 (2004).

322   35. Biraud, S.C., *et al*. A multi-year record of airborne CO_2 observations in the US Southern

323   Great Plains. *Atmos. Meas. Tech.* **6,** 751-763 (2013).

324   36. Huang, Y., Tan, X. & Xia, Y. Inhomogeneous radiative forcing of homogeneous

325   greenhouse gases. *J. Geophys. Res.* **121,** 2780–2789 (2016).

326   37. Jung, M., *et al*. Recent decline in the global land evapotranspiration trend due to limited

327   moisture supply. *Nature* **467,** 951-954 (2010).

328   38. Gero, P.J. & Turner, D.D. Long-term trends in downwelling spectral infrared radiance

329   over the U.S. Southern Great Plains. *J. Climate*. **24,** 4831-4843 (2011).

330   39. Willett, K.M., *et al*. HadISDH: an updateable land surface specific humidity product for

331   climate monitoring. *Clim. Past.* **9,** 657-677 (2013).

332   40. Dai, A. Recent climatology, variability, and trends in global surface humidity. *J. Climate*.

333   **19,** 3589-3606 (2006).

334   41. Berry, D.I. & Kent, E.C. A new air-sea interaction gridded dataset from ICOADS with

335   uncertainty estimates. *Bull. Amer. Meteor. Soc.* **90,** 645-656 (2009).

336   42. Simmons, A.J., Willett, K.M., Jones, P.D., Thorne, P.W. & Dee, D.P. Low frequency

337   variations in surface atmospheric humidity, temperature, and precipitation: Inferences

338   from reanalyses and monthly gridded observational data sets. *J. Geophys. Res.* **115,**

339   D01110 (2010).

340   43. Wentz, F.J., Ricciardulli, L., Hilburn, K. & Mears, C. How much more rain will global

341   warming bring? *Science*, **317**, 233–235 (2007).

342   44. Anderson, G.P., *et al.* AFGL atmospheric constituent profiles (0–120 km). AFGL-

343   TR_86-0110 (1989).

354

355 **Author Contributions:** D.R.F. led the research, performed all calculations, and wrote the

356 manuscript; W.D.C. proposed the study concept, provided research guidance, and conceived

357 methods for isolating the CH_4 signal; S.C.B. provided CH_4 and N_2O data and associated support;

358 M.D.R. provided the statistical analysis; D.D.T. provided guidance on AERI instrument

359 performance and research focus; P.J.G. helped interpret AERI data; J.T. analyzed

360 thermodynamic contributions to the observed forcing. D.H. provided C_2H_6 data and associated

361 support; S.X. provided ARMBE data and associated support; E.J.M. and T.R.S. provided clear-

362 sky error analysis; M.S.T. provided research feedback and guidance and served as P.I. of the

363 grant supporting this research. All authors discussed the results and commented on the

364 manuscript.

365

366 **Competing financial interests:** The authors declare no competing financial interests.

367 **Figure Captions:**

368

369 **Figure 1:** Recent evolution of atmospheric methane at the surface study site.

370 Time-series of the annual distribution of surface flask measurements of CH_4 at DOE ARM SGP

371 site. Box-whisker plots show the mean (+), median (line), the box bounding the 25- and 75-

372 percentile and the whiskers set at the 0.1- and 99.9-percentile for weekly flask measurements

373 from a given year. Least-squares linear trend analyses are included for selected time periods

374 before and after 2007 (vertical dashed line). The 2007 change-point was determined from weekly

375 time-series data (see Methods).

376

377 **Figure 2:** Factors affecting CH_4 longwave surface instantaneous radiative forcing.

378 (a) Change in spectral flux for a 1 ppbv perturbation in CH_4 for a 1 km layer in a Mid-Latitude

379 Summer (MLS) profile[44]. (b) Vertical sensitivity of downwelling surface flux in CH_4 absorption

380 band to 1 km perturbations in temperature, H_2O, N_2O, and CH_4 derived from LBLRTM radiative

381 transfer calculations with the MLS profile (c) Box-whisker diagrams of the vertical distribution

382 of CH_4 and N_2O, with inset of associated correlation coefficient in mixing ratio between the

383 surface and a given height, from aircraft observations[35] at SGP from flights 2002-2012. Box

384 spans 25th to 75th percentile, whisker spans 5th to 95th percentile of observations.

385

386 **Figure 3:** CH_4 longwave surface radiative forcing time-series.

387 Time-series (black), 2σ instantaneous uncertainty in CH_4 surface longwave radiative forcing

388 (gray; see Methods) and trends with 3σ uncertainty (red; ibid.) at DOE ARM SGP.

389

390   **Figure 4:** Thermodynamic dependence of CH_4 surface forcing.

391   (a) Vertically-resolved slope of ARMBE temperature measurements with the 99.7% confidence-

392   interval. (a) Same as (b) but for trends in the logarithm of specific humidity. (c) Surface radiative

393   forcing vs. tropospheric-averaged CH_4 as a function of temperature perturbations from 8 to 16.5

394   km from a mid-latitude summer atmosphere[44]. The change in mid-level temperature over the

395   observed time-period was 0.4±0.2 °K (99.7% CI) and is indicated on the plot (d) Same as (c) but

396   for humidity perturbations in g/kg from 0 to 1 km. The change in boundary-layer water vapour

397   over the observed time-period was -1.5±1.0 g/kg (99.7% CI) and is indicated on the plot.

398

399   **Figure 5:** Forcing time-series decomposition and reconstruction from predictors

400   (a) Time-series of CH_4 forcing signal noise removed by Random forest with 100 weak learners.

401   (b) Seasonal forcing signal. (c) Deseasonalized forcing signal. (d) Histogram of observed vs

402   decomposed and reconstructed forcing. (e) First component of Principal Component Analysis

403   (PCA) of temperature predictors (f) First component of PCA for humidity predictors. See

404   Methods for details.

Methods:

CH$_4$ surface radiative forcing was determined by differencing measured spectra from the AERI instrument[45], subject to quality control (see below), with radiative transfer calculations using 512 levels of temperature and humidity from radiosondes profiles as processed by the ARM Best Estimates (ARMBE)[33,46], ozone from the Modern-Era Retrospective Analysis for Research and Applications (MERRA)[47], CO$_2$ profiles from the nearest spatiotemporal grid point from CarbonTracker-CO2 2013[(48)], monthly-averaged N$_2$O mixing ratios from the Mauna Loa Observatory (MLO)[49], and pre-industrial (722 ppbv) CH$_4$ mixing ratios. This counterfactual calculation, designed to simulate the spectrally-resolved radiance field at the Earth's surface, had CH$_4$ mixing ratios remained at annually-averaged pre-industrial levels[27]. The counterfactual was created using the Line-by-Line Radiative Transfer Model (LBLRTM) version 12.2, using the AER line parameter database version 3.1[(50)] based on HITRAN 2008[(51)] with updated line-mixing[52] and the MT_CKD_2.5.2 H$_2$O continuum absorption model[25]. Limb-brightening factors, converting both observations and calculations from radiance to flux, were calculated with three-point Gaussian quadrature over zenith angle[53]. Supplementary Information Figure 1 shows a schematic of this process chain.

Data Quality Control

AERI spectra were recorded every 8 minutes from the instrument's initial deployment to April 2004 (at SGP). Subsequently, spectra were recorded every 30 seconds, with only minor outages, in order to provide higher temporal-resolution data for cloud studies[54]. This analysis only considered data starting in 2002 because the ARMBE data are derived from Vaisala RS-80 profiles prior to 2002 and that instrument suffered a known dry bias[55,56]. The end of the analysis

428   period was the start of 2013, which was chosen because the AERI instrument at SGP

429   experienced a failure and was replaced in mid-2013. The analysis could be extended beyond

430   early 2013 but would have to address complications from changing instrumentation[57].

431

432   Only the subset of spectra recorded within 2 hours of a radiosonde launch were utilized. With 4

433   daily launches, each measurement is separated by a minimum of 6 hours and spans 4 hours.

434   Based on the radiosonde profile, a radiance spectrum was calculated using LBLRTM with 512

435   levels of temperature and relative humidity from the ARMBE product[33]. All AERI spectra

436   recorded within 2 hours of the radiosonde launch were rank-ordered by the root-mean-squared

437   brightness temperature of the residual spectrum of the difference between the measurement and

438   the LBLRTM calculation between 600 and 980 cm^{-1}. This range was chosen to be sensitive to

439   thermodynamic conditions but insensitive to CH_4 or ozone, where the latter is strongly

440   influenced by MERRA biases[58]. The rank-ordered spectra were averaged sequentially together

441   (i.e., the first two spectra were averaged, then the first three spectra were averaged, etc.) and the

442   RMS of the residual between that average and the LBLRTM calculation was recalculated. The

443   sequential average of the spectra that produced the minimum RMS of the residual relative to the

444   radiosonde-based LBLRTM calculation was used as the AERI spectral measurement for

445   subsequent analysis. The rationale for this approach is to average as many spectra together as

446   possible to minimize random measurement error, but to avoid biasing the spectra by averaging

447   observations during which clouds were present or where the thermodynamic conditions had

448   changed relative to the radiosonde.

449

450   Since the determination of CH_4 surface forcing is so dependent on an accurate specification of

451   the atmospheric thermodynamic profile, we apply additional tests of the sequentially averaged

452   spectra against the counterfactual calculations to remove cases where the thermodynamic or

453   condensate profiles differ substantially between the observation and the counterfactual. First, we

454   evaluate the RMS of the residual between the AERI spectral measurement and the LBLRTM

455   calculation between 790 and 810 cm^{-1} (hereafter referred to as the 800 cm^{-1} channel), because

456   this region is sensitive to atmospheric temperature, humidity, and condensates (see

457   Supplementary Information Figures 2(a) and 2(b)). These plots show the slope and correlation

458   coefficient of the least-squares relationship between the radiative flux sensitivity to moisture and

459   temperature perturbations for a given channel outside the CH_4 absorption feature (1200-1350 cm^{-}

460   ^{1}) and the average radiative flux sensitivity to moisture and temperature perturbations within the

461   CH_4 absorption feature. The least-squares relationship is derived from six model atmospheres,

462   which span a wide range of terrestrial thermodynamic conditions[44]. The upper panels of Figures

463   (2a) and (2b) show that fluxes in the spectral region between 790 and 810 cm^{-1} are more

464   sensitive to perturbations in temperature and moisture than fluxes in the CH_4 absorption band.

465   The lower panels show that perturbations in temperature and moisture produce flux perturbations

466   in the 790-810 cm^{-1} spectral region and the CH_4 absorption band that are highly correlated.

467

468   We also utilize the RMS of the residual between 705 and 709 cm^{-1} (hereafter referred to as the

469   707 cm^{-1} channel), which is sensitive to the atmospheric boundary layer temperature.

470   Supplementary Information Figure 2(c) shows the gain and correlation coefficient for the

471   relationship between the variance of a spectral channel outside the CH_4 absorption feature and

472   the variance of the spectral channel within the CH_4 absorption feature, where both are calculated

473   with the measurements and calculations used in the aircraft validation cases (see below). This

474   figure shows that the 707 cm^{-1} variance is highly correlated with the variance within the CH_4

475   band across a range data wherein the 800 cm^{-1} tolerance criterion is satisfied below 5 K. A gain

476   of greater than unity, indicating high sensitivity to boundary-layer temperature perturbations, is

477   also shown at 707 cm^{-1} for the same 800 cm^{-1} tolerance criterion.

478

479   Only spectral residuals with an RMS residual spectrum brightness temperature at 800 cm^{-1} of

480   less than 3 K and a standard deviation at 707 cm^{-1} less than 0.3 K (after averaging) are

481   considered for subsequent analysis. See Supplemental Information for the rationale for these

482   threshold choices.

483

484   Supplementary Information Figure 4 shows the average residual spectrum featuring a large

485   deviation from zero where CH_4 has a prominent absorption due to the use of a pre-industrial CH_4

486   mixing ratio for the counterfactual calculation and deviations equivalent to less than 1 K in

487   temperature, 10 ppmv CO_2, 5% percent H_2O, and 10% N_2O. The exception lies in the 9.6 μm

488   ozone absorption band between 980 and 1080 cm^{-1}, indicating a systematic overestimation of

489   column ozone from the MERRA data products at SGP[58]. The lack of prominent spectral

490   structures outside the CH_4 and O_3 bands excludes other possible explanations including cloud

491   contamination, water vapour or temperature bias, or instrument calibration, all of which produce

492   spectral residuals with characteristic features not solely in the CH_4 absorption band.

493

494   **Time-Series Decomposition**

495   We tested the hypothesis that the cause for the observed trend in radiative forcing could be

496   contained within a set of predictors including height-resolved trends in water vapour, height-

497   resolved trends in temperature, and ground level methane concentration measured by flasks. If

498   we cannot use these predictors to reproduce the observed forcing, we can infer that there are

499   other contributing factors to the forcing that we have not considered. For the reconstruction of

500   this time-series, we used a two-step decomposition of all predictors using a widely utilized and

501   flexible approach that avoids overfitting[59]. First, we isolated the component of the unfiltered

502   signal that cannot be described as white noise or outlier data using a calibrated Random forest

503   with 100 weak learners[59]. A calibrated Random forest was used to reproduce the signal at the

504   desired points in time, and the difference between the reproduced and actual signal was filtered

505   out. Second, the remaining noise and cyclical components of the signal were removed using

506   moving average filter with a 12-month window[60]. The size of the moving-average filter window

507   was selected because the signal exhibited clear annual seasonal variations.

508

509   With this approach, we created a set of isolated trends for 1025 predictors (512 each for

510   temperature and humidity and 1 for flask CH_4 observations). To make the problem less

511   computationally expensive, and given the extreme level of redundancy in vertically-resolved

512   temperature and water-vapour predictors, we applied principal component analysis (PCA) for the

513   reduction of dimensionality[61]. The fraction of variance explain by the first 5 principal

514   components (out of 512) was found to be >99.99% for both temperature and humidity,

515   confirming the high-degree of redundancy in the predictors. With 5 PCs for temperature, 5 for

516   humidity, and 1 for methane concentration, we created a reduced set of 11 predictors to describe

517   the CH_4 radiative forcing trend. An ensemble of five back-propagation neural networks was then

518   trained to reproduce the trend component of the CH_4 radiative forcing[62]. To avoid over-fitting,

519   the training and reproduction of the radiative forcing was done in leave-one-out fashion, such

520   that the radiative forcing value to be reconstructed from the predictors is withheld from the

521   training set. Instead, ensemble neural networks are trained using the remaining data points, and

522   then the network is used to reproduce the withheld data point. The procedure was repeated

523   sequentially for all data points.

524

525   With this approach, the correlation coefficient between the observed trends in the entire CH_4

526   surface forcing time-series and the neural-network prediction where all 11 predictors are used is

527   0.9983 (R^2=0.997). Where only the CH_4 flask data is used as a predictor to train the network, the

528   correlation coefficient is 0.8907 (R^2 =0.793). More specifically, we can explain ~80% of the

529   variance in radiative forcing using custom-designed non-linear predictor. However, we should

530   note that our signal is obtained from the difference between an observation and calculation,

531   which is not best possible non-linear predictor, so the amount of variance that can be explained

532   using only CH_4 concentrations is necessarily less that 80%. Rather, our results produce an

533   estimate of the minimum of the fraction of variance that cannot be explained using the

534   predictor(s) of interest. They also show that information from temperature and humidity, and not

535   just CH_4 flask concentration data, is needed to describe the observed trend in CH_4 surface

536   radiative forcing.

537

538   **Statistical Analysis Methods**

539   The statistical analysis of the time-series seeks to determine whether and when a change point

540   occurred in the measured CH_4 surface radiative forcing, as well as the linear (temporal) trends

541   and their significance. The following describes the methods used to perform this analysis.

542

543   Define y_t as the CH_4 forcing for the SGP site at time $t = 1,\ldots, T$. Our statistical model is:

544

545    $y_t = b_0 + b_1 t + b_2 X_t (t - t_0) + a_j + e_t + v_t,$ (1)

546

547   where $\{b_k\}$ are unknown regression coefficients, $\{a_j\}$ represent (unknown) monthly effects, e_t are

548   independent and identically distributed (iid) $N(0, s^2)$ with s^2 unknown ($N(a, b)$ denotes a

549   univariate Gaussian random variable with mean a and variance b), and v_t iid $N(0, w^2)$ with w^2

550   known (also, e_t and v_t are independent). The model (1) contains two error processes: first, e_t

551   represents error in the model specification and therefore s^2 is estimated; second, v_t represents

552   error introduced by the measurement process on y_t and therefore w^2 will be considered fixed (see

553   Statistical Analysis Results). The variable X_t is defined to be 0 if $t \leq t_0$ and 1 if $t > t_0$, and the

554   change point must fall between fixed bounds $T_U < t_0 < T_L$. Therefore, for $t \leq t_0$, the monthly-

555   adjusted trend in expected CH_4 forcing has slope b_1; for $t > t_0$, the trend has slope $b_1 + b_2$.

556

557   The unknown parameters in (1) and the change point can be estimated using a common

558   (Frequentist) statistical technique called maximum likelihood (ML)[63], which also yields

559   confidence intervals for the regression coefficients[64]. Given the setup in (1), we can determine

560   the significance of the change point t_0 by way of model selection: the full model (1) can be   vs.

561    $H_1: b_2 \neq 0$). A test of H_0 can be done using a standard full vs. reduced model F-test for nested

562   models[64].

563

564   The Frequentist analysis described above ignores any uncertainty in estimating the change point,

565   and the model is not well suited to assess this uncertainty (outside of asymptotic evaluations)[65].

566   Alternatively, a Bayesian approach can be used to determine the significance of the change point

567   while accounting for its uncertainty (again using model comparison). Bayesian models that

568   mirror the full (1) and reduced (2) models can be set up using noninformative prior distributions

569   and estimated using Markov Chain Monte Carlo (MCMC) methods[66]. MCMC output can be used

570   to compare the full and reduced models using Bayes factors[67].

571

572   **Statistical Analysis Results**

573   The aforementioned models were fit for many different data sets from the SGP site. This data set

574   was created by using values of the 800 cm^{-1} brightness temperature (BT) residual threshold

575   parameter ranging from 0.1 to 10 (see Data Quality Control). However, if the data set for a

576   particular threshold value had fewer than 50 observations, the analysis was not conducted. The

577   upper and lower limits of the change point were fixed to $T_L = 2004$ and $T_U = 2010$; any potential

578   change points near the beginning or end of the time series are not of interest. The seasonal cycle

579   of CH_4 due to hydroxyl radical destruction is captured via the monthly effects $\{a_j\}$; for

580   comparison, all models were fit and results presented both with and without the monthly effects.

581

582   For the ML models, plots of the estimated change point, significance of the change point, and

583   estimates of the slope parameters (with 99.7% confidence intervals) from both before and after

584   the change point are provided in Supplementary Information Figures 5 and 6. Results from the

585   Bayesian models were approximately identical to the ML models and are omitted. Based on the

586   similarity of results, the main text used the more familiar Frequentist results including the

587   monthly adjustment.

588

589   Supplementary Information Table 1 numerically summarizes the results of the statistical analysis

590   used in the main text where the 800 cm^{-1} BT threshold is 3 K.

591

592   **Controlling for N_2O**

593   The methods used to determine CH_4 surface radiative forcing can be biased by N_2O. Figure 2(b)

594   shows this due to the substantial amount of overlap in spectral radiance changes from

595   perturbations from N_2O and CH_4. However, the vertical profiles of N_2O collected by the ARM-

596   ACME missions[35] at SGP show that N_2O mixing ratios at altitude are highly vertically-correlated

597   with the surface (see insets of Figure 2(c)) and vary by less than 1 ppbv seasonally.

598

599   Moreover, these differ very little from measurements at MLO. The error incurred in CH_4 forcing

600   from utilizing monthly-averaged MLO N_2O observations instead of in situ ARM-ACME N_2O

601   observations was maximized at 1.2% of the CH_4 forcing.

602

603   N_2O can still bias CH_4 forcing because it is emitted after precipitation following the nearby fresh

604   application of nitrogen-based fertilizer[68], causing >5 ppbv deviations from the background N_2O

605   mixing ratio. NEXRAD data[69] were used to screen data to remove those observations for which

606   precipitation had occurred in the previous 24 hours.

607

Instantaneous Error

There are several sources of error in the determination of the surface forcing from the AERI

measurements. They include (1) spectroscopic error in LBLRTM; (2) AERI measurement error;

(3) error in the temperature, water vapour, CO_2, or O_3 inputs to LBLRTM inputs; and (4) a

contribution of unknown aerosol or cloud condensates to the AERI observations. While the error

contributions from (1) are outside of the scope of this analysis, we can perform a top-down

estimate of errors from (2) through (4) with AERI measurements and LBLRTM calculations

using inputs from simultaneous aircraft profiles.

616

Surface radiative forcing time series from the aircraft data were derived from differencing AERI

observations with counterfactual calculations. These were compared with the surface radiative

forcing time series computed by differencing an LBLRTM calculation with the aircraft-observed

profile of CH_4 and N_2O and the counterfactual calculation.

621

Supplementary Information Figure 8 show the standard deviation of AERI-observed and aircraft-

derived surface radiative forcing. Figure 3 shows that an abscissa value of 3 K corresponds to an

ordinate value of 0.14 W/m^2, which is thus our estimate of the 1-σ instantaneous error in

radiative forcing.

626

Ethane Data Analysis

Supplementary Information Figures 9(a) and 9(b) show time-series analyses of ethane (C_2H_6)

flask data. Non-Methane Hydrocarbon (NMHC) flask data from SGP were first filtered for

630   outliers; values that deviated more than 2-σ from a running median were excluded from trend

631   analyses. Filtered data were then uploaded to the NOAA server for filtering and trends were

632   determined using the method of Thoning et al.[70]

633

634   **Clear-Sky Bias**

635   We evaluate the potential for clear-sky bias in the determination of CH_4 surface radiative

636   forcing. We estimate this bias by recalculating the Broadband Heating Rate Profile (BBHRP)[71]

637   profiles at SGP for 2010 based on pre-industrial CH_4 mixing ratios and comparing those to the

638   original BBHRP profiles, containing time-varying CH_4 derived from the nearest grid box from

639   CarbonTracker-CH4[72]. We then subset the data identified as clear-sky in the Radiatively

640   Important Parameters Best Estimate (RIPBE) product[73].

641

642   We find that most of the forcing is in the clear-sky but that the all-sky surface forcing is 0.065

643   W/m^2, or 33%, less than the clear-sky forcing. This finding is expected because of non-negligible

644   overlap between broadband cloud absorption and CH_4 absorption, thereby masking CH_4 forcing.

645   This cloud-masking may vary year-to-year. Currently, the independent estimates of cloud

646   vertical profiles produce residual spectra with signatures of clouds, so the effect of CH_4 cannot

647   be isolated under all-sky conditions.

648

649   **Non-Methane Contributions to Observed Signal**

650   The possibility that condensates or non-methane gaseous atmospheric constituents are

651   contributing to the observed CH_4 surface forcing must be considered. The contribution of

652   condensates can be excluded because they produce broadband signals that are not observed in the

653   residual spectra. We can also address the non-methane gaseous constituent question by

654   determining the effects of perturbations in the atmospheric concentrations of 32 additional

655   species with spectroscopy tabulated in HITRAN[21], and found their contributions to be at least 5

656   orders of magnitude smaller than CH_4.

657

658   **Flasks-Based Observations**

659   At the SGP site, a pair of 2.5 liters glass flasks is collected on a weekly basis from the top of the

660   central facility 60m tower. Flask collection started in April 2002 and is currently ongoing. The

661   collection of a pair of flasks allows basic quality assessment and control. These observations are

662   part of the NOAA's Global Greenhouse Gases Reference Network (REF)[74]. Flasks are collected

663   in the afternoon, when the planetary boundary layer is well-developed and observations are

664   representative of a large area. Aircraft profiles of CH_4 and N_2O were recorded on approximately

665   a bi-monthly basis from 2002 until the present (see Supplementary Information Figures 7(a) and

666   7(b)).

667

668   Ground-based and aircraft-based flasks are analyzed after they are collected at NOAA/ESRL by

669   gas chromatography, and measurements are reported against WMO CH_4-X2004 and N_2O

670   X2006A scales. Flask-based observations are shown to have uncertainties of less than 1.2 ppbv

671   for CH_4 and 0.4 ppbv for N_2O.

672

673   **Aircraft Validation**

674   Aircraft profiles of CH_4 and N_2O above the SGP site were recorded on approximately a weekly

675   basis with flask observations from 2002 until the present. Prior to 2006, the flasks were

676   collected only at 0.6 and 3.6 km, but since then, flasks were collected at 12 elevations between

677   0.5 km and 5.5 km above sea level (see Supplementary Information Figures 7(a) and 7(b)).

678

679   **Single-Site Analysis**

680   The analysis presented here focused on the SGP site. Several other ARM sites exist, including

681   the North Slope of Alaska (NSA) site, and AERI data from that site was analyzed for previous

682   work[27]. For the CH_4 analysis, however, differences in the instrumental noise in the AERI

683   instrument at NSA greatly complicated the analysis there. In particular, the Extended—Range

684   AERI at NSA has an expanded spectral range compared to the AERI at SGP, leading to higher

685   instrumental (random) noise over 1200-1350 cm^{-1} spanning the dominant CH_4 absorption

686   feature[75].

687

688   **Residual Brightness Temperature Threshold Rationale**

689   The rationale for choosing a threshold of 3 K brightness temperature is based on balancing the

690   number of data points with error in the CH_4 surface forcing determination, both of which will

691   increase with increasing threshold values. Another related factor for the determination of an

692   appropriate threshold is the importance of observations throughout the year. The 3 K threshold

693   enables a determination of the seasonal cycle in surface forcing at the SGP site and summertime

694   multi-year trends at the NSA site. Supplementary Information Figure 3 shows the relationships

695   between the 800 cm^{-1} brightness temperature residual threshold and the number of data points.

696

697   **Data Availability**

698   The ARM data and radiative transfer codes used in this analysis are freely available to download

699   from http://www.archive.arm.gov/discovery/ and http://rtweb.aer.com, respectively. The

700   following are URLs from which input data can be downloaded:

701   MERRA: http://goldsmr3.sci.gsfc.nasa.gov/opendap/MERRA/MAI3CPASM.5.2.0/contents.html

702   CarbonTracker-CO2: ftp://aftp.cmdl.noaa.gov/products/carbontracker/co2/molefractions/

703   CarbonTracker-CH4: ftp://aftp.cmdl.noaa.gov/products/carbontracker/ch4/molefractions/

704   NOAA CH_4 data: http://ds.data.jma.go.jp/gmd/wdcgg/pub/data/current/ch4/

705   NOAA N_2O data:

706   ftp://aftp.cmdl.noaa.gov/data/hats/n2o/insituGCs/CATS/daily/mlo_N2O_Day.dat

707   NOAA C_2H_6 data: http://ds.data.jma.go.jp/gmd/wdcgg/pub/data/current/vocs/ethane/event/

708   Reprints and permissions information is available at http://www.nature.com/reprints

709

710   **Code Availability**

711   The computer code developed for this research was written in Matlab and will be made available
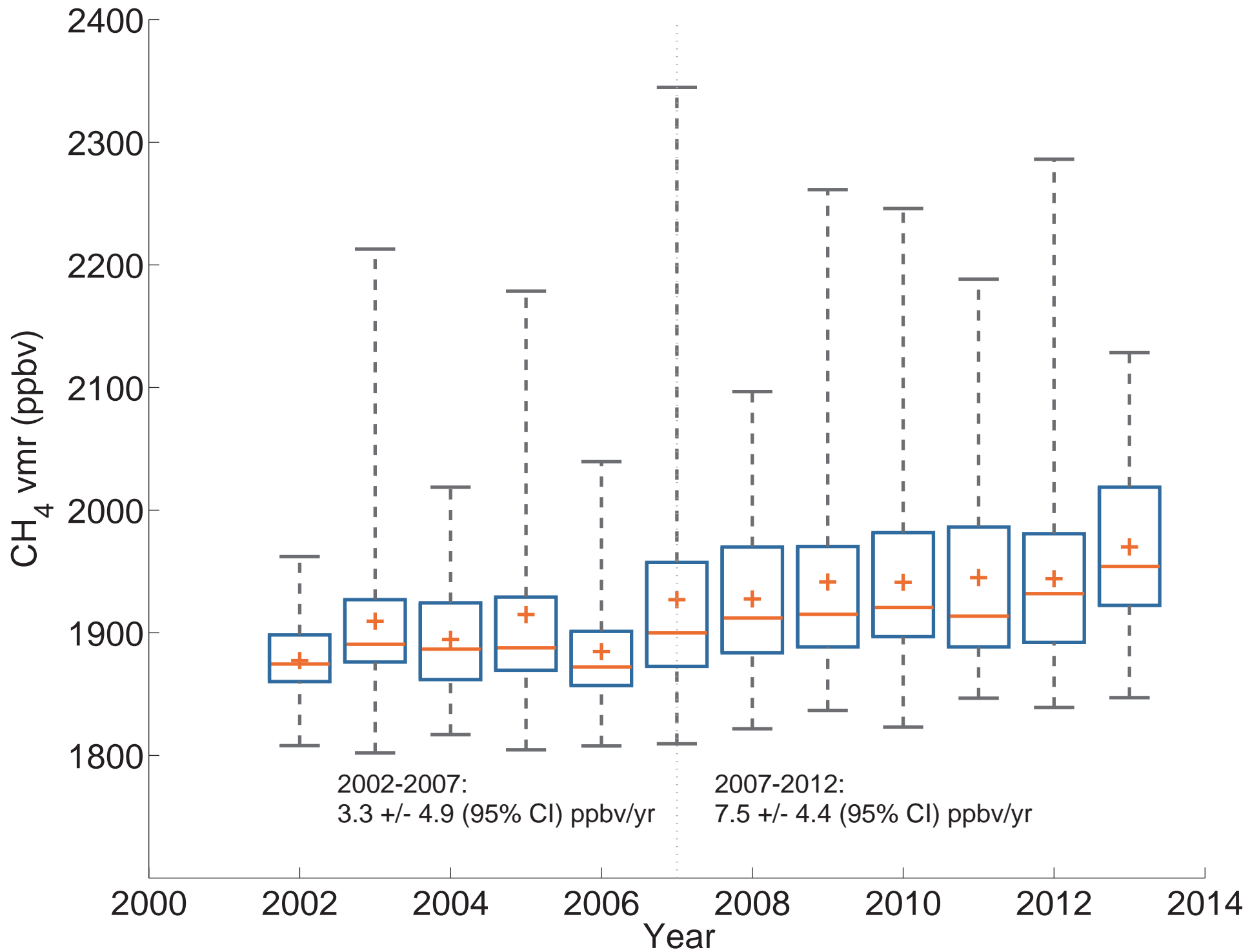
712   upon request.

References:

45. Atmospheric Radiation Measurement (ARM) Climate Research
    Facility. 1994, updated **hourly**. Atmospheric Emitted Radiance Interferometer
    (AERICH1). **2000-01-01** to **2015-06-01**, **36.605 N 97.485 W: Southern Great Plains**
    (SGP) Central Facility, Lamont, OK (C1). Compiled by J. Gero, B. Ermold, A.
    Koontz, K. Gaustad, D. Hackel and R. Garcia. Atmospheric Radiation Measurement
    (ARM) Climate Research Facility Data Archive: Oak Ridge, Tennessee, USA. Data set
    accessed **2015-06-01** at http://dx.doi.org/10.5439/1025143.

46. Atmospheric Radiation Measurement (ARM) Climate Research
    Facility. 1994, updated **yearly**. ARM Best Estimate Data Products
    (ARMBEATM). **2012-01-01** to **2012-12-31**, **36.605 N 97.485 W: Southern Great**
    Plains (SGP) Central Facility, Lamont, OK (C1). Compiled by X. Chen and S.
    Xie. Atmospheric Radiation Measurement (ARM) Climate Research Facility Data
    Archive: Oak Ridge, Tennessee, USA. Data set accessed **2015-06-**
    01 at http://dx.doi.org/10.5439/1039931.

47. Rienecker, M.M., *et al.* MERRA: NASA's Modern-Era Retrospective Analysis for
    Research and Applications. *J. Climate* **24,** 3624–3648 (2011).

48. Peters, W., *et al.* An atmospheric perspective on North American carbon dioxide
    exchange: CarbonTracker. *Proc. Natl. Acad. Sci. USA*. **104,** 18925-18930 (2007).

49. Nitrous Oxide data from the NOAA/ESRL halocarbons in situ program. Calibration
    scale used: NOAA 2006A More information about the calibration scale can be found at:
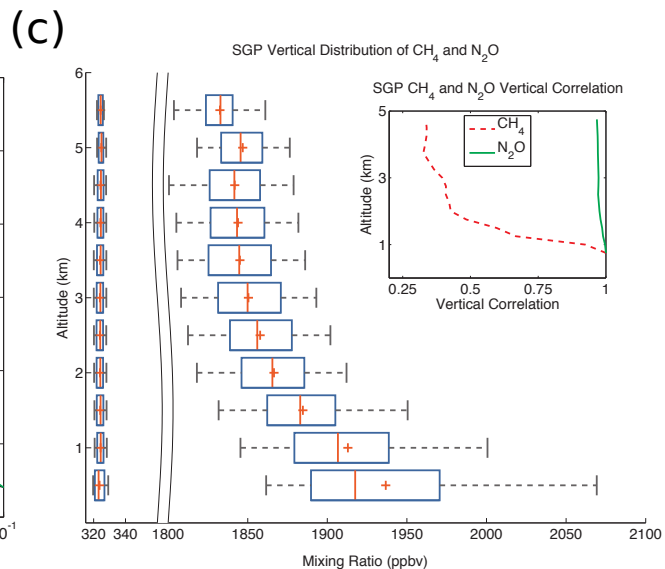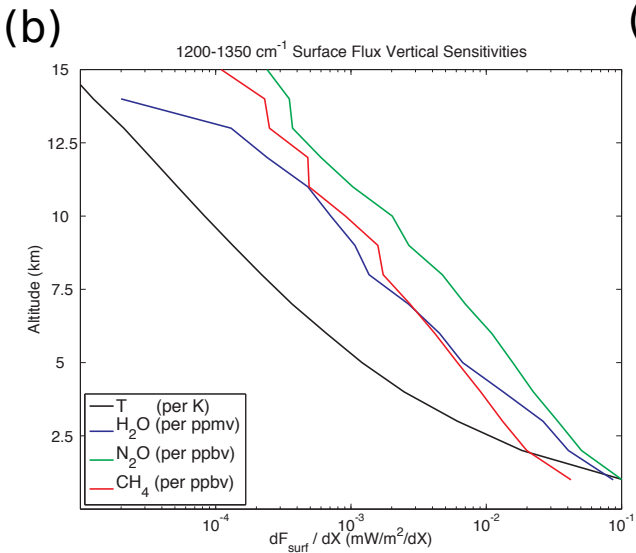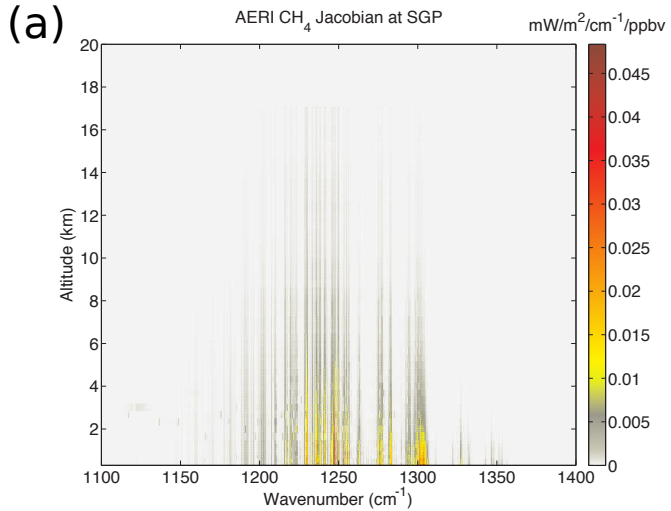   http://www.esrl.noaa.gov/gmd/ccl/

735   50. Clough, S.A., *et al*. Atmospheric radiative transfer modeling: a summary of the AER

736   codes. *J. Quant. Spectrosc. Rad. Trans*. **91,** 233-244 (2005).

737   51. Rothman, L.S. *et al.* The HITRAN 2008 molecular spectroscopic database, *J. Quant.*

738   *Spectrosc. Rad. Trans.* **110,** 533-572 (2009).

739   52. Alvarado, M.J., *et al.* Impacts of updated spectroscopy on thermal infrared retrievals of

740   methane evaluated with HIPPO data. **8,** 965-985 (2015).

741   53. Li, J. Gaussian Quadrature and Its Application to Infrared Radiation. *J. Atmos. Sci.* **57,**

742   753–765 (2000).

743   54. Turner, D.D., Knuteson, R.O., Revercomb, H.E., Lo, C. & Dedecker, R.G. Noise

744   Reduction of Atmospheric Emitted Radiance Interferometer (AERI) Observations Using

745   Principal Component Analysis. *J. Atmos. Oceanic. Technol.* **23**, 1223-1238 (2006).

746   55. Wang, J., *et al.* Corrections of Humidity Measurement Errors from the Vaisala RS80

747   Radiosonde – Application to TOGA COARE Data. *J. Atmos. Oceanic Technol.* **19,** 981-

748   1002 (2002).

749   56. Turner, D.D., *et al.* Dry bias and variability in Vaisala radiosondes: The ARM

750   experience. *J. Atmos. Oceanic Technol.* **20,** 117-132 (2003).

751   57. Weatherhead, E.C., *et al*. Factors affecting the detection of trends: Statistical

752   considerations and applications to environmental data, *J. Geophys. Res.*, **103,** 17149-

753   17161 (1998).

754   58. Liu, X., *et al.* OMI Ozone Profile and Tropospheric Ozone and Cross Evaluations with

755   Chemical Transport Models, *AGU Meeting of the Americas*, A31A-22 (2013).

756   59. Kuhn, M. & Johnson. K. *Regression trees and rule-based models in Applied Predictive*

757   *Modeling* (Springer, New York, 2013).

758   60. Shumway, R.H. & Stoffer., D.S. *Time Series Analysis and Its Applications*. (Springer,

759   New York, 2000).

760   61. Ivosev, G., Burton, L. & Bonner, R. Dimensionality reduction and visualization in

761   principal component analysis. *Anal. Chem.* **80**, 4933 (2008).

762   62. Frank, R.J., Davey, N. & Hunt, S.P. Time series prediction and neural networks. *Journal*

763   *of Intelligent and Robotic Systems*. **31**, 91–103 (2001).

764   63. Casella, G. & Berger, R.L. *Statistical Inference Ch. 7.2.2* (Duxbury Press, Ithaca, NY,

765   (2002).

766   64. Ravishanker, N. & Dey, D. *A First Course in Linear Model Theory* (Chapman and

767   Hall/CRC, 2002).

768   65. Casella, G. & Berger, R.L. *Statistical Inference Ch. 10.4* (Duxbury Press, Ithaca, NY,

769   (2002).

770   66. Gilks, W.R., Richardson, S. & Spiegelhalter, D.J. *Markov Chain Monte Carlo in Practice*

771   (Chapman and Hall/CRC, 1995).

772   67. Kass, R. E. & Raftery, A.E. Bayes Factors. *J. Am. Stat. Assoc.* **90,** 773-795 (1995).

773   68. Bouwman, A.F., Boumans, L.J.M. & Batjes, N.H. Modeling global annual N_2O and NO

774   emissions from fertilized fields. *Global Biogeochem. Cy.* **16,** 1080 (2002).

775   69. Fulton, R.A., Breidenbach, J.P., Seo, D.J., Miller, D.A. & O'Bannon, T. The WSR-88D

776   Rainfall Algorithm. *Wea. Forecasting*. **13,** 377–395 (1998).

777   70. Thoning, K.W., Tans, P. P. & Komhyr, W. D. Atmospheric carbon-dioxide at Mauna Loa

778   observatory .2. analysis of the NOAA GMCC data, 1974-1985. *J. Geophys. Res.* **94,**

779   8459-8565 (1989).

780   71. Mlawer, E.J., *et al.* The broadband heating rate profile (BBHRP) VAP. *Proc. 12th ARM*

781   *Sci. Team Meet.* ARM-CONF-2002, US Department of Energy (2002).

782   72. Bruhwiler, L.M., *et al.* CarbonTracker-CH4: an assimilation system for estimating

783   emissions of atmospheric methane. *Atmos. Chem. Phys.* **14,** 8269–8293 (2014).

784   73. McFarlane, S., T. Shippert, J. Mather. (2011). Radiatively Important Parameters Best

785   Estimate (RIPBE): an ARM value-added product. DOE Tech. Rep. SC-ARM/TR-097 US

786   Department of Energy.

787   74. Dlugokencky, E.J., Steele, L.P., Lang P.M. & Masarie, K.A. The growth rate and

788   distribution of atmospheric methane. *J. Geophys. Res.* **99,** 17021-17043 (1994).

789   75. Knuteson, R.O., *et al.* Atmospheric Emitted Radiance Interferometer. Part II: Instrument

790   Performance. *J. Atmos. Ocean. Technol.* **21,** 1777–1789 (2004).

SGP CH$_4$ Flask Measurements Box-Whisker Plot

(a) AERI CH$_4$ Jacobian at SGP — mW/m²/cm^{-1}/ppbv

(b) 1200-1350 cm^{-1} Surface Flux Vertical Sensitivities

T (per K)
H$_2$O (per ppmv)
N$_2$O (per ppbv)
CH$_4$ (per ppbv)

(c) SGP Vertical Distribution of CH$_4$ and N$_2$O

SGP CH$_4$ and N$_2$O Vertical Correlation

CH$_4$
N$_2$O

SGP CH$_4$ Forcing

2002-2007: -0.003 ± 0.006 W/m^2/yr

2007-2012: $+0.026 \pm 0.006$ W/m^2/yr

CH$_4$ Forcing (W/m^2)

Year

(a) SGP ARMBE Vertical Temperature Trend 2002-2012

Legend:
- Trend 2002-2007
- Trend 2007-2012
- 2002-2007 95% CI
- 2007-2012 95% CI

x-axis: Temperature trend (K/yr)
y-axis: Altitude (km)

(b) SGP ARMBE Vertical Humidity Trend 2002-2012

Legend:
- Trend 2002-2007
- Trend 2007-2012
- 2002-2007 95% CI
- 2007-2012 95% CI

x-axis: Humidity trend ((log g/kg)/yr)
y-axis: Altitude (km)

(c) CH_4 Surface Forcing vs. Mid-Level T Perturbation

x-axis: CH_4 Tropospheric Mixing Ratio (ppbv)
y-axis: 8-16 km T perturbation (K)
colorbar: W/m^2

(d) CH_4 Surface Forcing vs. Boundary Layer H_2O

x-axis: CH_4 Tropospheric Mixing Ratio (ppbv)
y-axis: 0-1 km H_2O perturbation (g/kg)
colorbar: W/m^2

(a) Noise removed by Random Forests (RF)

(b) Seasonal Component of CH$_4$ Surface Forcing

(c) Deseasonalized CH$_4$ Surface Forcing

(d) Histogram of Obs. vs. Reconstructed CH$_4$ Forcing

(e) First Temperature Reconstruction Eigenvector: 99.985 %

(f) First Humidity Reconstruction Eigenvector: 99.947 %